University of Cincinnati

Date: 3/27/2014

I, Huayan Liang , hereby submit this original work as part of the requirements for the degree of Master of Science in Mechanical Engineering.

It is entitled:

Evaporation Enhancement for Condensational Nanoparticle Growth in Hydrophobic Evaporation - Condensation Tube

Student's name: **Huayan Liang**

This work and its defense approved by:

Committee chair: Sang Young Son, Ph.D.

Committee member: Pramod Kulkarni, D.Sc.

Committee member: Frank Gerner, Ph.D.

10431

Evaporation Enhancement for Condensational Nanoparticle Growth in Hydrophobic Evaporation - Condensation Tube

A thesis submitted to the
Graduate School of the University of Cincinnati
in partial fulfillment of the requirements for the degree of

Master of Science

in the Department of Mechanical & Materials Engineering
of the College of Engineering & Applied Science

by

Huayan Liang

B.A. Tsinghua University, Beijing, China, 2009

Committee: Sang Young Son, Ph.D.
Frank M. Gerner, Ph.D.
Pramod Kulkarni, Ph.D.

Abstract

In present study, the enhancement of meniscus evaporation by changing meniscus shape and area was investigated. Rather than observing the meniscus shape directly, an alternative method has been utilized. A Condensation Particle Counter (CPC) structure, which benefits from meniscus evaporation of a porous media to make vapor for water droplet growth, has been introduced to analyze the production water droplet. By analyzing the size and concentration of the condensed water droplet from CPC, the enhancement of meniscus evaporation taken place at the porous media was determined. The meniscus shape and area alterations were controlled by applying an additional pressure onto the meniscus. The results of the bigger condensed water droplet and higher concentration clearly demonstrate that the enhancement has been achieved to the meniscus evaporation, which was led by changing of the additional pressure applied to the meniscus of the porous media.

Acknowledgements

As the end of my Master's period, I would like to express my appreciation to my advisor Dr. Sang Young Son. Dr. Son has been quite supportive to allow me conduct my adventures in his lab. I was instructed and persuade to conduct experiments to verify my own point of view. Also leant the lesson from all mistakes I made and stuffs I broke. I had opportunities to argue and discuss with him frankly and I can keep my views at the same time. His instructions supported me step forward towards the success.

I would like to offer my gratitude also to my committee members Dr. Frank Gerner and Dr. Pramod Kulkarni for their comments and suggestions on my piece of work which made my consideration more comprehensive.

I would like to thank all members of Micro Thermo Fluidics Laboratory, Dr. Lee, Dr. Kim, Dr. Anand Sushant, Michaerl Martin, and Hai Fu. It was you who made my study life plentitude and colorful. And thank all of you for the supports and suggestions to my work.

I would like to thank my family and friends who always stay with me through my entire life, supporting me and encourage me to overcome any difficulties. I love you all.

List of Figures

List of Tables

Contents

1. Introduction

1.1 Overview

The problem of evaporation from a water-vapor meniscus in a micro-scale channel has been discussed in various fields, especially in micro heat pipes and steady vaporization systems in channels (Ha & Peterson, 1998). In a wetting film case, the evaporation rate is dominated by great temperature gradients near the gas-liquid contact line (Morris, 2003). The heat transfer processes taken place at the liquid-gas meniscus rely on the latent heat released by vaporization of certain liquids to supply high enough local heat fluxes such as what happens in heat pipes. Also it is well known high heat transfer rates is presented in systems of evaporating meniscus, thus, the quantitative description of the heat transfer and evaporation process in the meniscus, and the determination of secondary parameters such as pressures on the meniscus and meniscus surface area remain matters of considerable interests.

Wayner and co-workers have published papers on experimental observations results of evaporating meniscus (Wayner, 1974), indicating that fluid fed to the drop base of the meniscus leads to an enlargement to the radius of the meniscus curvature. Wayner’s later work noted that the same conclusion can be drawn by investigating heat transfer characteristics of the meniscus at the outlet of a capillary tube (Wayner, 1976). Renk and Wayner (Renk and Wayner, 1977) executed experiments utilizing interferometry theory to examine an evaporating meniscus suspended at the gap between two flat plates placed horizontally, and concluded that the pressure gradients of water flow fed to the droplet was associated by a gradient in the meniscus curvature, accompanied with the significant increases in the heat flux. Deryaguin argued that the evaporation rate at meniscus, which brought by the pressure gradient from a changing film thickness, could enhanced by several times of that caused merely by diffusion (Deryaguin, 1965). Later work done by Churaev and Ershova adopted the previou model and observed the evaporation rate in hydrophilic capillaries was higher than that in hydrophobic capillaries (Chureav, 1971). Mathematical analyses of meniscus evaporation phenomena are still in the development stage. Potash and Wayner (Potash, 1972) modeled the heat and mass transport processes happening in an evaporation meniscus which formed on a heated vertical flat plate. They suggested that a better model to describe the actual meniscus profile should include a transition region with curvature effects.

Rather than observing the meniscus shape and area directly, the usage of a structure which designed by the meniscus evaporation principal can be an alternative method to analyze the evaporation enhancement on the meniscus. By analyzing the production of the droplets which required evaporated vapors from the meniscus, the enhancement of evaporation of the liquid-gas meniscus can be obtained. Condensation Particle Counters (CPCs) were one of the products that benefit from meniscus evaporation. A porous media in between the liquid and gas fields in CPCs provides meniscus evaporated vapor, which is used for droplet heterogeneous nucleation. One of the main destinations of the CPCs is to make the droplet grow, which is mainly due to the thermodynamic conditions inside the growth tube structure. A supersaturation condition is needed by the droplet heterogeneous nucleation and the condition is approached by evaporated water vapor from the evaporative wall of the growth tube. The evaporation physics in a capillary porous media have been studied and analyzed for decades, and numerical models have been under development.

During the evaporation process of CPCs, porous media is utilized for wicking fluid from the reservoir to the evaporation section. This action in combination with the evaporation of the working fluid in evaporation section causes the fluid to transport. The heat and mass transfer characteristics of the gas-liquid interface meniscus are characterized by the conduction resistance of the liquid and the exposed surface area of the meniscus for evaporation (Ranjan, 2009). The evaporation heat and mass transfer from the gas-liquid interface meniscus has been modeled under such condition by the same author (Ranjan, 2010). Quantification work on wick performance in terms of evaporation rates has been finished (Iverson, 2007), in which the thermal resistance for evaporation of different porosity copper wicks on thin layers was measured experimentally under saturated vapor condition (Davis, 2008). In previous studies, it is believed that the thin film evaporation, which takes place at the gas-liquid interface, dominates the heat and mass transfer. The thin film evaporation has been reported to affect the overall heat and mass transfer in porous media (Hanlon, 2003). In a theoretical model developed by Wang *et al*. that it has been forecasted that the heat transfer occurred in the thin film supplied more than 50% of the total from the evaporating meniscus (Wang, 2007).

1.2 In This Study

In present work, the meniscus evaporation enhancement effected by meniscus shape and area change has been studied. By indirectly analyzing a CPC's performance, which utilizes the vapor evaporation from meniscus of porous media for water droplet growth, the enhancement of meniscus evaporation can be determined.

A new structure, Evaporation-Condensation Tube (ECT), is proposed using non-wetting porous media as the core of the CPC. In the previous work of our group, the operability of this device has been tested at different flow rates and water temperatures by determining the detection efficiency, condensation droplet size, and cross section droplet size distribution at the cross sectional area of the tube exit (Anand and Son, 2012). The vapor distribution inside the ECT possesses nucleation capability for the particles as small as 2-100 nm, and the numerical studies reveal that a 20 nm particle can grow to 3-4 μm in less than 60 ms. In the present project, the previous work has been extended through evaluating the performance of ECT by changing the meniscus interface evaporation area which is approached by applying an additional pressure on the gas-liquid interface of the pores on the ECT wall. The applied additional pressure would enhance the resulting vapor evaporation rate through the porous media and increase the supersaturation of the vapor by affecting the contact angle and gas-liquid meniscus interface area. The enhancement to the evaporation due to such meniscus evaporation area enlargement would cause the increase of residence time for the condensation droplet inside the supersaturation field and thus leads to a larger condensed droplet size. Smaller particles that had not grown big enough for detection would be activated under the improved condition. Therefore, more activated droplets would result in the increase of the detection efficiency of CPCs.

2. Methodology

2.1 Heterogeneous Nucleation

Most of the water based CPCs are using the principle of heterogeneous nucleation to obtain the condensation droplets for optical detection.

In general, heterogeneous nucleation requires establishment of a non-equilibrium state, which gives rise to natural forces resulting in atomic gradients and mass transport effects (Ohring,M 2002). A system is in non-equilibrium state when thermal or concentration gradients exist. These concentration gradients result in the sticking of molecules to the solid surface, and are accompanied by processes such as adsorption, surface diffusion, or chemical binding at the surfaces. In a vapor system, the non-equilibrium state can be expressed in terms of its partial pressure in relation to the saturation pressure at a particular temperature. When the partial pressure of the available vapor is greater than the amount of vapor that can be held at a given temperature, the state of the system is supersaturated. The supersaturation ratio is defined as the quotient of the vapor partial pressure to its saturation pressure at a particular temperature, given by

$$S = p_A / p_s(T) \qquad (1)$$

For the given thermal conditions inside the CPC device, a saturation ratio will be fixed and minimum sized nanoparticles which can be activated and detected is used. The distributions of the saturation ratio inside the ECT have been depicted (Anand & Son, 2011).

2.2 Meniscus Interface

2.2.1 Formation

In a porous media as the evaporation condensation tube (ECT), capillary pressure is the force necessary to support a droplet through a pore and is higher for smaller pore diameter. Pressure difference across the liquid surface exists and is expressed as:

$$P_c = P_{non-wetting} - P_{wetting} \tag{2}$$

The above equation also can be expressed by surface tension, contact angle, and pore diameter as:

$$\left(P_{non-wetting} - P_{wetting}\right)\frac{\pi}{4}D^2 = \sigma_{LG}\cos(\theta_{contact})\,\pi D \tag{3}$$

$$P_c = 4\sigma_{LG}\frac{\cos(\theta_{contact})}{D} \tag{4}$$

Where σ is the surface tension of the water which is 7.2 x 10^{-2} N/m, θ is the contact angle with the pore, and D is the pore diameter which is R= 10^{-6} m.

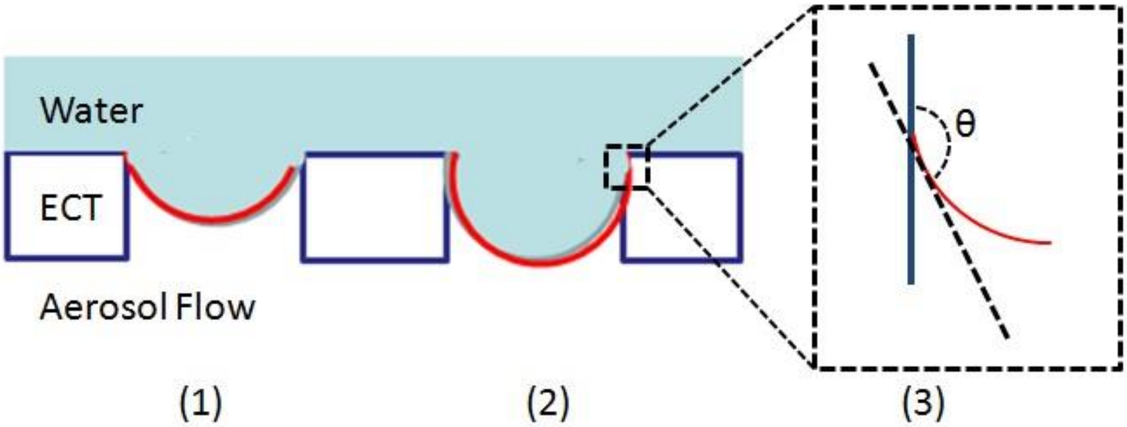

Figure 1. Meniscus Gas-Liquid Interface Area Change of the ECT (1) No additional pressures added (2) Additional pressure added (3) Contact angle

Figure 1 shows the schematic diagram of the meniscus gas-liquid interface area change by applying additional pressure. The ECT can be considered as a porous media, thus the capillary pressure will form a meniscus inside the pore and this structure is where the evaporation occurs. When the additional pressure applied on the gas-liquid interface, it can be inferred from equation (4) that the contact angle is the only parameter which would vary under the condition of identical pore size and water temperature. The change of the contact angle will cause a different exposure surface for evaporation. Additional pressure applied on the interface will cause the exposure surface of meniscus to increase, thus the water vapor evaporation area has been enhanced and the performance of the CPC is improved. The detailed calculation for the shape and evaporation area variation of the meniscus interface would be described below.

2.2.2 Meniscus Interface Evaporation

The evaporation takes place at the meniscus gas-liquid interface of the porous wall of ECT. In the evaporating meniscus model inside a channel discussed by Ma & Peterson (1998), the meniscus evaporation interface is a concaved meniscus shape and the evaporation rate was controlled by the temperature gradients near the gas-liquid contact line. Due to the shape of the concaved meniscus, a wetting film exists at the contact line and the phase interface turns parallel to the wall. The evaporation occurs mainly on the wetting thin film for the concaved meniscus evaporation interface (Ajaev & Homsy 2001). For any meniscus that curves away from a wall when contact angle is small, the heat flow and evaporation are determined by the contact region. The heat flow which decides the evaporation rate is related solely with the contact angle. Thus, the relationship among the evaporation condition, interface curvature, and contact angle is established (Morris, 2003).

The evaporation mass flux reaches the peak near the contact line. Approximately more than 80% of the total evaporation from the meniscus interface takes place at a small area which is about 20% of the total meniscus area, identified as the thin-film area (Ranjan, 2010). The evaporation heat and mass flux from the gas-liquid meniscus interface decreases with the increasing of the contact angle as a result of the corresponding decreases in this thin-film area when the contact meniscus is in concaved shape (contact angle smaller than 90 degree).

For the cases in present experiment with a convex meniscus interface exists, while the thin-film area is almost vanished with the contact angle greater than 90 degree, the evaporation rate is determined exclusively by the area of the convex meniscus interface. Therefore, the surface area of the meniscus will reflect the evaporation condition.

In present work, the meniscus interface area and evaporation rate of the ECT are discussed under the following assumptions.

1. The vapor phase above the gas-liquid interface is saturated.
2. The gas-liquid meniscus interface is static during the process of evaporation. This conjecture is reasonable because of the feeding water rate is sufficient to make up the evaporation rate at the interface.
3. The evaporation process happens uniformly at the whole meniscus surface. Thus the relation between the surface area of the meniscus and the evaporation rate is established.

2.2.3 Meniscus Interface Area Estimation Calculation

The shape of the meniscus gas-liquid interface in a pore is ellipse. The surface area estimation is made as the simplified condition, under which a droplet condensed on a flat surface.

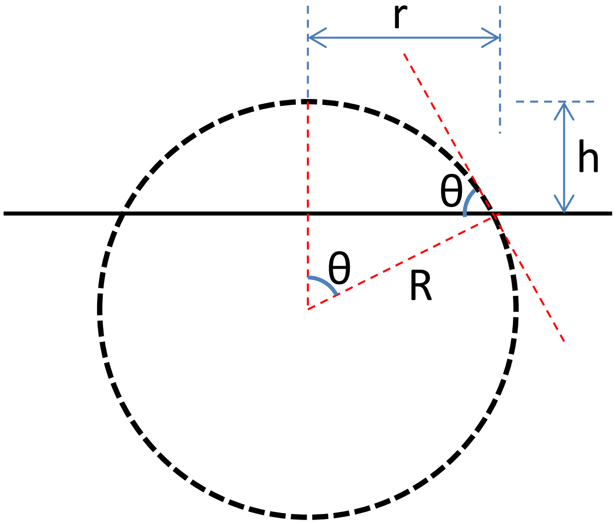

Figure 2. Droplet condensed on a flat surface

Figure 2 shows that a droplet condensed on a surface. The part of liquid is in a shape of spherical cap. If r refers to the droplet's base radius, R refers to the radius of curvature of the droplet, and h refers to the height of the droplet sitting on the surface, the spherical cap surface area is given as

$$A = 2\pi Rh \tag{5}$$

Where,

$$h = R - R\cos\theta \tag{6}$$

$$R = r/\sin\theta \tag{7}$$

Assuming the condensed base area is fixed, the r is a constant. Then the spherical cap surface area A can be expressed by a function of contact angle θ as

$$A = \frac{2\pi r^2}{cos\theta} \tag{8}$$

Equation (8) derives the relationship between the contact angle and the pressure difference at interface as

$$P_{non-wetting} - P_{wetting} = 4\sigma \frac{\cos\theta}{D} \tag{9}$$

If the ellipsoid shape droplet at the pore of porous media is regarded as spherical, the meniscus shape interface surface area could be estimated by previous equation and a relationship between the meniscus interface surface area and additional pressure applied could be found.

In the experimental case, by applying an additional pressure ΔP, the $P_{wetting}$ becomes $\left(P_{wetting} + \Delta P\right)$. The diameter of the pore D is the diameter of the base, then

$$D = 2r$$

Therefore, the relationship between the meniscus interface surface area and the additional pressure applied can be given as

$$A = \frac{4\pi r^2 \sigma}{2\sigma + r[P_{non-wetting} - (P_{wetting} + \Delta P)]} \tag{10}$$

Where under a certain temperature, the surface tension of the water to air σ and the pressures beside both side of the interface, $P_{non\text{-}wetting}$ and $P_{wetting}$, can be treated as constants.

The relationship of the meniscus area A with additional pressure applied ΔP is plotted with Mathematica as shown in Figure 3. The calculation uses constants values as:

Surface tension of water to air at 60˚C, $\sigma = 6.62 \times 10^{-2} N/m$. Pore radius $r = 0.92\ \mu m = 9.2 \times 10^{-7} m$. $P_{\text{non-wetting}} = 101325$ Pa and $P_{\text{wetting}} = 101525$ Pa.

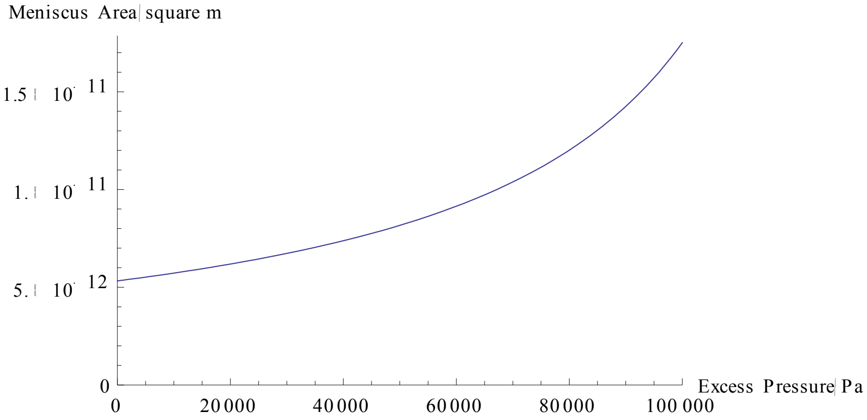

Figure 3. Relationship between Meniscus Interface Area and Applied Additional pressure

The surface area of the meniscus interface raises faster when the applied additional pressure increases. The limitation of the additional pressure from the mathematical estimation can be reached by making the denominator of equation (10) be zero. The limitation of the additional pressure for the previous case is $\Delta P_{max} = 1.437 \times 10^5$ Pa as shown in Figure 4 calculated by Mathematica.

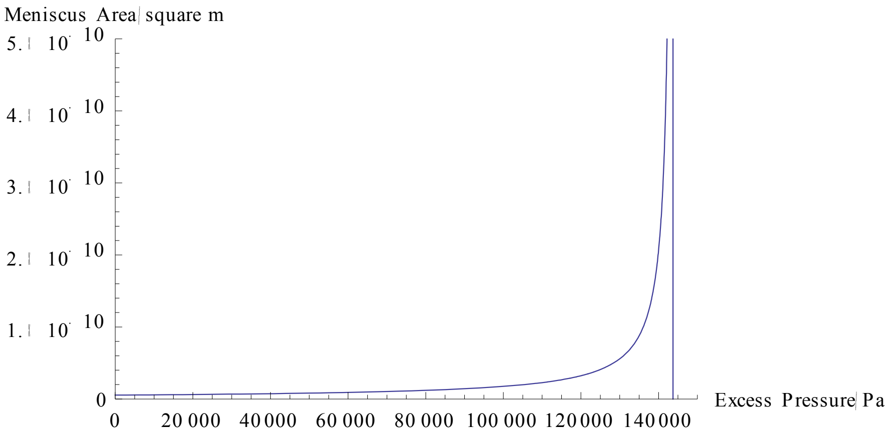

Figure 4.Relationship between Meniscus Interface Area and Applied Additional pressure with the Limitation of Applied Additional pressure

2.3 Experimental Setup and Procedures

2.3.1 Evaporation Condensation Tube

ECT is the core structure of our CPC. As shown in Figure 5(1), the ECT is a non-wetting porous media which is used to separate the working fluid and the aerosol flow containing particles, while supplying a path for the water vapor to access the gas region for the condensation process. Table 1 listed the properties of the non-wetting porous media.

Meniscus interface is formed inside the pores between the working fluid water and the aerosol gas carrying particles. The capillary pressure is constructed to maintain the meniscus. The parameter in the present study is the additional pressure added on the interface. To achieve a static, stable and convenient setup, the water jacket is connected with a water tower to control the additional pressure. The pressure of the static water tower, which is a 2 cm diameter tube with scales on its side, is transported to the ECT interface by the principle of communicating vessels. By controlling the height of water level in the water tower, the pressure applied on the gas-liquid interface meniscus can be adjusted precisely and stably.

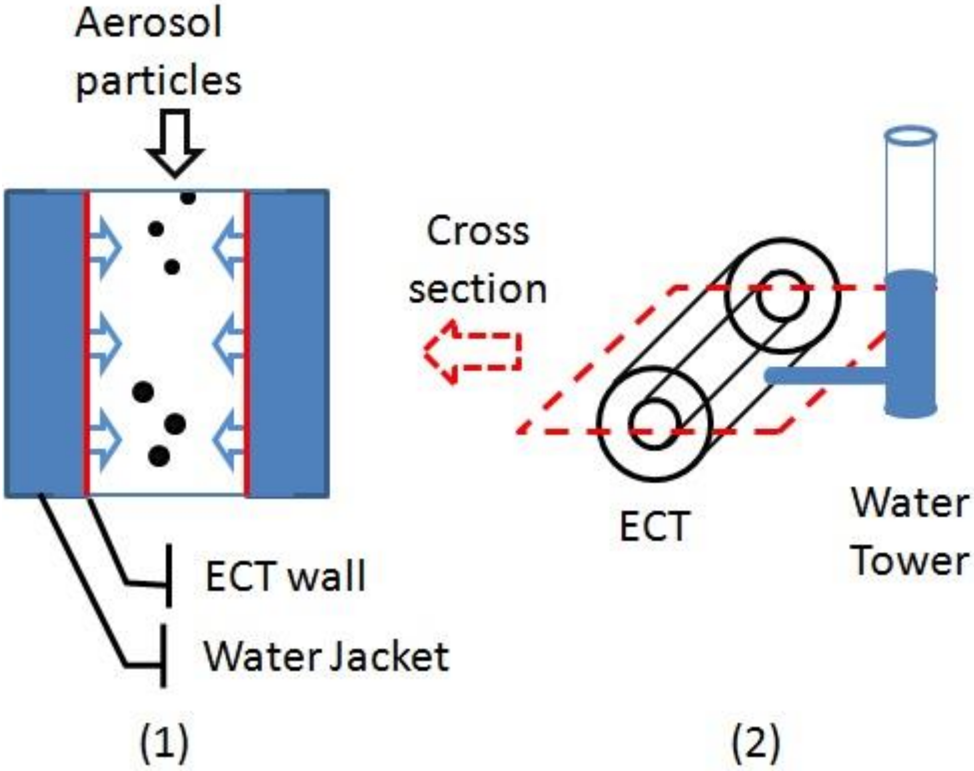

Figure 5. Schematic of ECT structure (1) Cross section area of ECT (2) ECT connection with water tower.

Table 1. Properties of non-wetting porous media

Material properties	Values
Average pore size	0.45 μm
Porosity	70 %
Burst Through Pressure	62000 Pa
Contact angle (Water, 101.3 kPa, 298K)	130.7 degree
Thickness	130 μm
Tube outer diameter	6 ± 0.2 mm
Tube length	30 mm

2.3.2 Experiment Procedures

The experiment setup consists of three different functional parts, the monodisperse particle generation and selection unit, the thermodynamic condition monitoring and controlling unit, and the signal capturing unit (Figure 6).

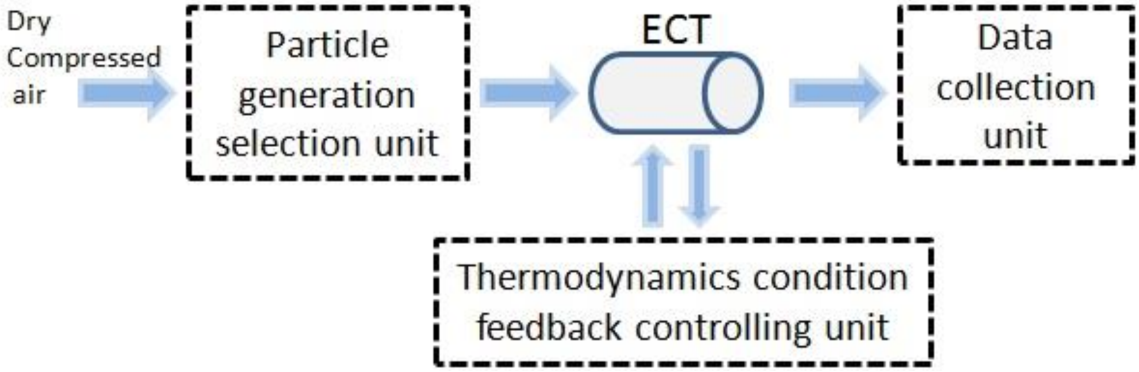

Figure 6. Schematic flowchart of the experiment setup

2.3.2.1 Monodisperse Particle Generation Selection Unit

The schematic diagram of monodisperse particle generation and selection unit is shown in Figure 7. The dash line area is the Aerosol Generator and Monitor system MSP 1500 (MSP Corp.). Dry compressed air was supplied into the system through a single jet collision type atomizer (Figure 7(1)) filled with sodium chloride solution with the NaCl concentration of 0.1%. After passing through a dryer (Figure 7(2)), the aerosol would be singly charged by the electrical corona ionizer (Figure 7(3)) and sent to the Differential Mobility Analyzer (DMA), (Figure 7(4)). The DMA is capable of classifying particles in the size range from 8 to 1000 nm. The classified particles neutralized by a Po-210 neutralizer (Figure 7(5)) passed through a water saturator (Figure 7(7)) to increase the relative humidity, and were supplied to the ECT for condensational heterogeneous nucleation. A comparison flow carried the same condition aerosol was sent back to the 1-Butanol CPC (Figure 7(6)) inside the MSP 1500 which would provide the reference value for the particle concentration to evaluate the detection efficiency of the ECT.

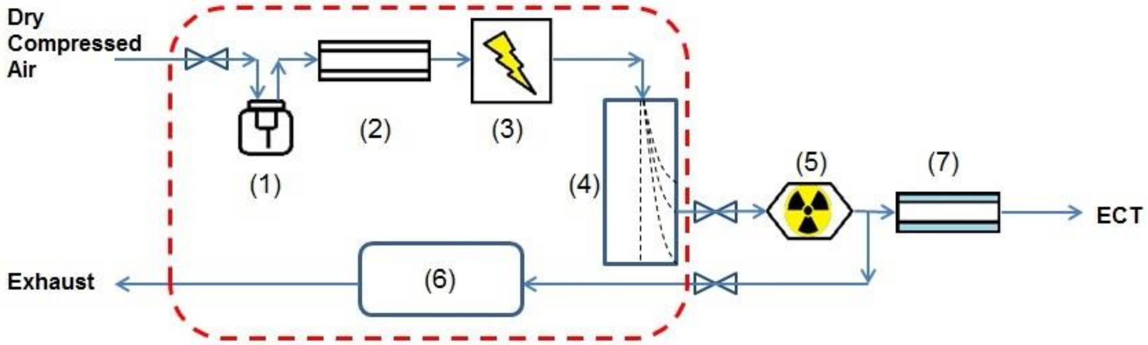

Figure 7.Schematic diagram of the particle generation and selection unit. (1) Atomizer. (2) Dryer. (3) Electrical Ionizer. (4) DMA. (5) Po-210 Neutralizer. (6) Butanol CPC. (7) Water Saturator. The structure in dash area is the device MSP 1500. (MSP Corp.)

In the present investigation, the source particles were generated from 0.1% NaCl solution using the atomizer of MSP 1500. The particle size distribution of the NaCl solution was measured by MSP 1500 using a continuously changing scan voltage method, and is shown in Figure 8. The particles having the maximum abundance are the ones with the size range around 20 nm. To maintain a stable concentration and sufficient numbers in the experiment, 20 nm size particles were used as the source particles in this experimental study.

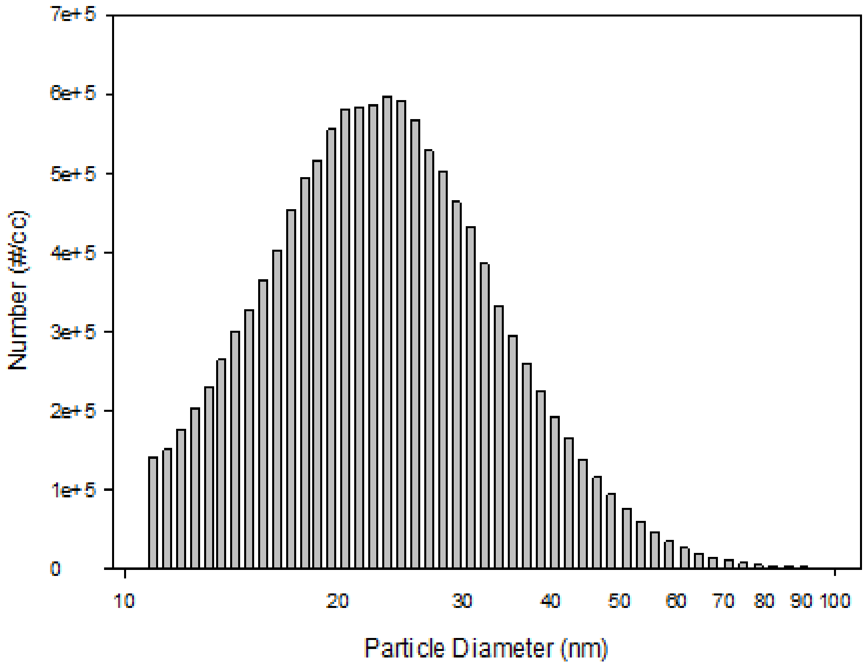

Figure 8. 0.1% NaCl solution source particle size distribution measured by MSP 1500 (MSP Corp.)

2.3.2.2 Thermodynamic Condition Control Unit

The thermodynamic condition is the most important unit for a CPC. The control and monitoring of the thermodynamic condition for the experiment is attached on the ECT. In Figure 5(1) the cross sectional structure of a condensation tube is shown. Water was filled in the water jacket and spiral shaped heating elements were placed inside the water to control the temperature. The aerosol carried with monodisperse particle flowed in the ECT. K-type thermocouples were applied along the length of the ECT to measure the water temperature and the average of these measurements was used as the ECT wall temperature. The temperature was gathered by data acquisition unit (34970A, Agilent Technologies) and controlled by varied power supply voltages monitored by a

Proportional Integral Derivative (PID) program built with the LabVIEW software. The flow rate of the aerosol was monitored by the mass flow meter TSI 4140 (TSI. Inc.) and manually adjusted. The enlargement of the meniscus area was regulated by applying an additional pressure onto the interface. A static water head, which supplied the additional pressure on the meniscus of ECT, was connected to the water jacket as shown in Figure 5(1), and could be adjusted easily and precisely by measuring and varying the water cylinder height.

2.3.2.3 Data Collection and Analysis Unit

The information of the grown particles generated from the ECT was collected by the particle visualization system and recorded by a CCD camera (Sensicam QE, LaVision) as shown in Figure 9.

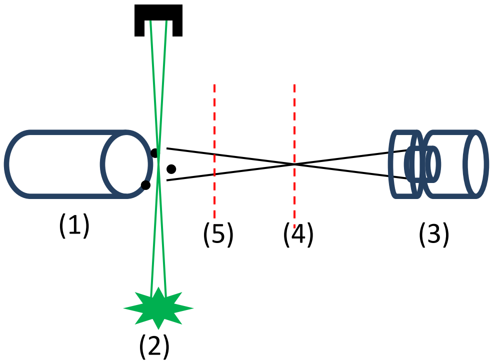

Figure 9. Schematic of the Particle Visualization Data Collection and Analyze Unit (1) ECT (2) Nd:Yag 532nm Laser (3) CCD Camera (4) Focus Plane (5) Out-of-focus Plane

The laser applied was a pulsed Nd:YAG laser (SoloII-30, New Wave Research) with 532 nm wavelength at illumination time 3-5 ns and at a frequency of 30 Hz. The laser beam was reduced to a laser sheet with thickness of 400 μm through a combination of lenses (LaVision). The laser sheet was located 1 mm away from the outlet plane of the ECT, which was the minimum distance to avoid the evaporation of the grown droplets after the exit of ECT when contacted with the surroundings at room temperature. The CCD camera (Sensicam QE, LaVision) was placed facing the outlet and at the same level as the ECT. The whole cross sectional area of the exit plane of ECT was covered and illuminated by the laser beam and the scattering light of the condensed particles were captured by the camera using the timing program. The recorded images carried the information of the grown droplets such as the concentration, location, and sizes of the droplets.

The distance between the camera and ECT exit plane could be adjusted. As in Figure 9(4) and (5), the camera was placed at the focus plane and out-of-focus plane separately to gather different messages. The information of condensed droplets gathered at focus plane was the concentration of the aerosol, while single droplet size data could be obtained at out-of-focus plane. Details of the capture and analyze methods at each plane are given below.

2.4 Concentration Measurement and Detection Efficiency Calculation Method

Ultrafine particles from sodium chloride solution were supplied by MSP 1500 as described above. The flow rate, inlet droplet size, water jacket temperature, and additional pressure on ECT were controlled. After aerosol flow passed the ECT, the condensed droplets were recorded by the CCD camera.

When the camera was placed at the focused position where the focal plane overlapped with the laser plane, the light scattered by every single droplet could be identified as a clear dot due to the extremely short exposure time (3 to 5 ns). An image analyzing software Image J (National Institute of Health) was applied to count and analyze the number of the shining dots on each picture.

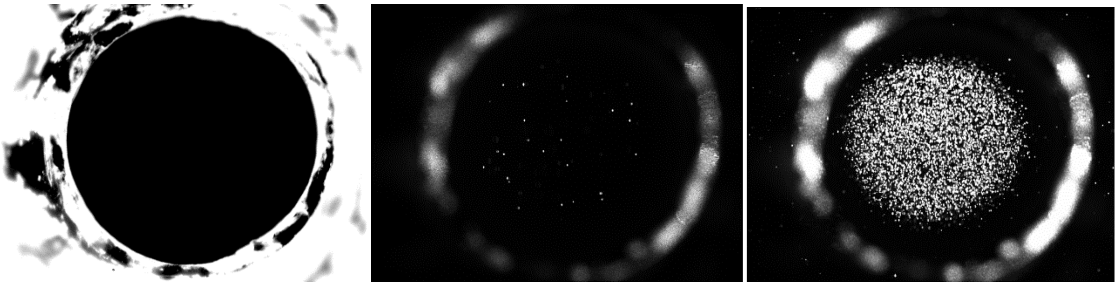
(1) (2) (3)

Figure 10Figure 10. Camera recorded pictures at the exit plane of ECT.

Figure 10 shows the set of typical recorded and analyzing procedure. Before particles were supplied, the camera distance was adjusted to make the focus of the ECT exit as shown by Figure 10(1). The exit shape of the ECT was recorded and the area was calculated by using the scale of the camera view. During the experiment, the camera was set to take pictures by the sampling rate of 50 pictures per minute and 400 pictures per set. Figure 10(2) is one of the pictures. The small dots were the scattered laser light by the condensed droplets and they were randomly distributed in the range of the exit plane. After recording, all pictures were analyzed by the Image J software. Background noise threshold cutting, brightness and contrast readjustment, and sharpening of the droplets boundary were presented on each picture by a programed bench process. The number of clear dots on each picture was measured by the Image J. By multiplying the exit area and the laser beam thickness, the shining volume was obtained. Quotient of the average dots based on 400 pictures and the shining volume was the droplets concentration of one experiment run, defined as detection concentration. By comparing this with the reference concentration measured by the 1-Butanol CPC in MSP 1500, which is calibrated with a

Model 3068B Aerosol Electrometer (TSI Inc.) beforehand, the detection efficiency of the ECT was acquired.

2.5 Droplet Size Measurement by Interferometric Mie Imaging Method

When the CCD camera was moved away from the ECT slightly, the scattering condensed particles were located in the out-of-focus plane of the camera. With a 5mm diameter circle aperture mounted to the camera, instead of showing as clear shining dots, the scattering condensed particles appeared as interferometric fringe patterns. The sizes of the condensation droplets could be calculated from the information carried by these fringe patterns by Interferometric Mie Imaging (IMI) method (Ragucci, 1990). Figure 11 shows typical captured images of the out-of-focus fringe patterns and droplet sizing result after the calculation by LaVision IMI software.

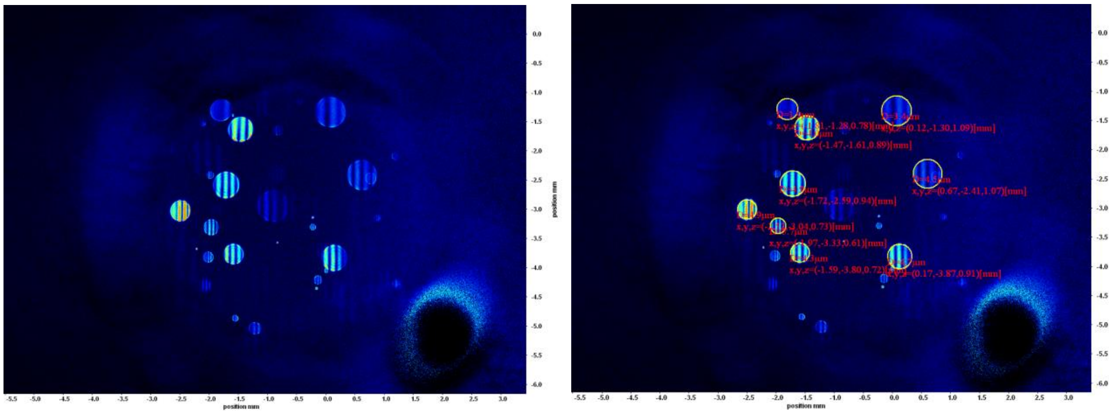

Figure 11. Sample recorded images of condensed droplet size fringe patterns and IMI droplet size calculation results.

The Interferometric Mie Imaging technique is a method that observes the interference of the particle image spots on the out-of-focus plane. The fundamental principle of this technique was based on Mie scattering. In general, the out-of-focus image was used to see the interference fringes and these fringe patterns were not present in the in-focus position. The fringe patterns existed because of the constructive and destructive interference of the light which was scattered from the particles. When light passed through the droplets it was reflected and refracted, leading to a phase shift of the light wave. Therefore in the out-of-focus images, the light passing through the aperture of the camera lens interfered with each other and the droplets images turned into a fringe pattern. The droplet diameters were post processed by evaluating the distance and number of the fringe patterns.

The calculation of the droplet size from the number and distance between fringe patterns could be simplified as the following.

After calibration and scaling, we have following parameters:

α= 0.00653 pixel/mm (scaling of the image)

n=1.33 (refractive index)

λ=532nm (laser wavelength)

θ=90° (observation angle)

M=0.988 (magnification)

f=84.8mm (lens focal distance)

de=42 mm (distance from aperture to object)

Then do the following calculations.

The distance from the object to the lens a:

$$a = \frac{f(M+1)-e\frac{h}{H}}{M-\frac{h}{M}} \tag{5}$$

The distance from the aperture to the lens e:

$$e = f\left(1+\frac{1}{M}\right) - de \tag{6}$$

The observation angle 2ω:

$$2\omega = 2\arctan\left(\frac{H}{2(a-e)}\right) \tag{7}$$

The fringe spacing Δ ϕ:

$$\Delta\phi = \Delta\phi_{pixel}\frac{2\omega}{h_{pixel}} \tag{8}$$

The diameter of the particle d:

$$d = \frac{2\lambda}{\Delta\phi}\left[\cos\frac{\theta}{2} + \frac{n\sin\frac{\theta}{2}}{\sqrt{1+n^2-2n\cos\frac{\theta}{2}}}\right]^{-1} \tag{9}$$

Same as the experiments for aerosol concentration, the experiments for condensed droplet sizes also took 400 image per set by the speed of 50 images per minute. The size of every single condensed droplet on each image was calculated by the LaVision software and the average was recorded for the specific thermodynamic condition.

2.6 Polystyrene Latex Particle Calibration to Validate the IMI Calculation

The size of the condensed droplet calculated from the IMI method is dependent on the angle and distance measurements being measured with high precision. Errors made on the physical measurement would influence every measured droplet size. To minimize the error from measurement and improve the accuracy of the calculation method, a Polystyrene Latex (PSL) particles measurement calibration was conducted whenever the ECT required detachment and re-attachment to the experiment setup to correct the error brought by distance variation.

PSL particles calibration was performed with same ECT and under same flow rate. PSL particles (PD2000 and PD3000, Duke Scientific) with the size of 2.01±0.04 μm and 3.04±0.06 μm were applied as the source particles and the out-of-focus images were captured and analyzed by the LaVision software.

For each size PSL particles, three sets of experiments were conducted and 400 images were recorded in each. The calculated size of the PSL particle was averaged from every single fringe pattern from the scattering particles. Since the PSL particles have specific size within small range (2.01±0.04 μm and 3.04±0.06 μm), when the calculated result was away from this range, the IMI calculation parameters in the software was adjusted until the result fell into the expected range. Thus, the IMI calculation parameters were accurate enough to calculate the condensed droplets with unknown sizes from the ECT at the adjusted camera location.

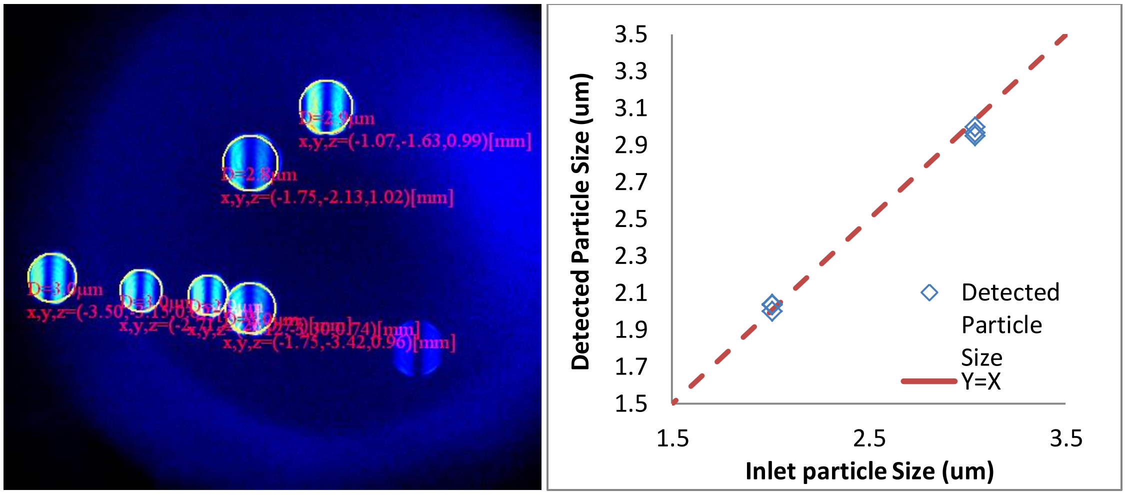

Figure 12. PSL particle calibration sampling image and calibration result.

Table 2. PSL particle calibration results.

Inlet particle Size(µm)	Detected Particle Size(µm)
2.01±0.04	2.023±0.020
3.04±0.06	2.978±0.044

Figure 12 shows a sample IMI calculation image of 3 µm PSL particles. Within this image, the particle sizes were ranged from 2.8 µm to 3.0 µm. Table 2 shows the result of the calibration which is the average of three sets of experiments for each PSL particle size. The calibration result was linear for different PSL particle sizes, indicating that the modified IMI calculation parameters were commonly accepted for all droplet size calculations under the same camera distance setup.

2.7 Experiment Uncertainty

Various parameters were controlled and measured in this experiment, therefore the experimental uncertainty was important to consider.

The uncertainty in the temperature measurement of the K-type thermocouple was ±1 K, while the K-type thermocouple itself had 0.75% of error. Wall temperatures of ECT were maintained to be within ±0.5 K controlled by the PID and the inlet air temperature was preserved as 298 ± 2 K. The accuracy of the flow meter (TSI 4140, TSI, Inc.) reading was within ±2%. Inlet particle concentrations were controlled by MSP1500 and total concentrations were limited to be lower than 10000 particles/cc to minimize the coincidence effect. In the image analysis procedure, the uncertainty associated with analysis of out-of-focused images to calculate droplet sizes was found to be less than 5%, which was mainly induced by droplet coincidence.

3. Results and Discussion

In general, the incoming aerosol flow entered the ECT at a lower temperature in an unsaturated form while the inside wall of the tube was at a higher temperature. The water vapor concentration was fully saturated at the inside wall of the ECT and the incoming aerosol vapor species concentration was less; thus, the vapor and energy were transferred from the ECT wall to the centerline of the ECT. The transfer rates of the energy and vapor were distinct because of the concentration gradient difference. The higher transfer rate happened at the entrance of the ECT where the largest temperature and concentration gradient were located.

The energy transfer rate versus mass transfer rate is given by Lewis Number which shows the ratio between thermal diffusion and mass diffusion. The Lewis Number value for water vapor is less than 1 which means the energy transfer happens slower than the mass transfer. The water vapor at the wall with a higher temperature would diffuse towards the centerline where the incoming air had a lower temperature and water vapor concentration. However, since the temperature increment was smaller than the concentration increment, the saturation vapor pressure was lower. Thus, the supersaturation condition could be built up rapidly from the inlet of the ECT.

The supersaturation condition is the major reason for the condensed particle growth. Various parameters, such as wall temperature, aerosol flow rate, and the incoming saturation ratio, were studied and optimized by previous research studies (Franklin, 2010; Hering, 2005; Anand, 2011; etc). Actually all of these parameters are associated with improving the evaporation rate of the water vapor from the porous media. Also several studies focused on the porous media evaporation rate improvement by analyzing the drop wise evaporation condition related to contact angle, curvature, and contact line motion. (Shripad, 2002)

Bourges *et al.* studied the influence of evaporation for drops of water placed on various substrates, and stated that the drop evaporation could be split into four stages (Bourges, 1995). Compared with our case, since the water jacket was fed with water continuously, the pressure between the gas phase and liquid phase of the gas-liquid interface meniscus could be considered as stable. The pressure balance maintained the shape of the meniscus which meant a stabilized contact angle existed. Also the surrounding atmosphere was saturated with water vapor during the evaporation which retained the contact angles to be constant.

Under such conditions, since the shape of the gas-liquid interface meniscus was preserved, the evaporation rate would also not change. The variations made on the gas-liquid interface including contact angle, curvature, and contact line motion could be explained by the interface surface area alteration. From the methodology chapter, the shape of the meniscus is determined by the balance of the wetting pressure and non-wetting pressure. The additional pressure applied on the gas-liquid interface meniscus in present experiments was a unique method to adjust the shape and surface area of the meniscus; therefore influenced the evaporation rate of the porous media so that the performance of the ECT was strengthened.

The experiments conducted in this study mainly focused on the change of the meniscus gas-liquid interface evaporation area by varying the additional pressure applied on the interface via the adjustment of the height of the connected water head. The parameters chosen were 5 cm, 15 cm, and 25 cm water heads which led to 490 Pa, 1471 Pa, and 2452 Pa pressure applied, respectively. Based on the properties given in Table 1, a pressure that smaller than the burst through pressure 62000 Pa could be applied. However, a pressure higher than 3000 Pa deformed the ECT and caused leakage inside the condensation tube due to the limitation of strength at the connection of the ECT and the plastic structure tube.

In all cases, the aerosol flow rate was selected as 0.3 liter per minute and continuous change of wall temperatures was applied to examine the effect of the additional pressure in all thermodynamics conditions.

3.1 Evaporation Enhancement by Meniscus Interfacial Area Change

Evaporation conditions play the key role for droplet growth. The experiments were performed with an additional pressure applied on the meniscus gas-liquid interface to introduce an area change; consequently, an evaporation enhancement was accomplished.

With the assumption made in session 3.2.2, the evaporation uniformly occurred on the elliptic area of the meniscus. The shape of the interface was simplified as a spherical cap and the area change was calculated. Under the present experiment conditions, the additional pressures were applied as 490 Pa, 1471 Pa and 2452 Pa.

The variations of contact angles and corresponding meniscus interface areas introduced by the additional pressure were calculated using the surface tension for water to air at 60˚C, $\sigma = 6.62 \times 10^{-2} N/m$, pore radius $r = 0.92\,\mu m = 9.2 \times 10^{-7} m$, $P_{\text{non-wetting}}$ = 101325 Pa, and P_{wetting}=101425 Pa.

The increase rates of the contact angle and meniscus interface area were calculated to be 0.22%, 0.65%, 1.08% and 0.34%, 1.03%, 1.73% with applied additional pressures of 490 Pa, 1471 Pa, 2572 Pa, respectively, as shown in Figure 13. The evaporation condition was solely dependent on the meniscus interface area according to the assumptions in session 3.2.2; therefore, the application of the additional pressure caused the enhancement of the evaporation rate. With the additional pressure applied, the interface area increase rate was higher than the contact angle increase rate. An expected estimation could be made that with even higher pressure applied, the enhancement of the evaporation condition would increase significantly.

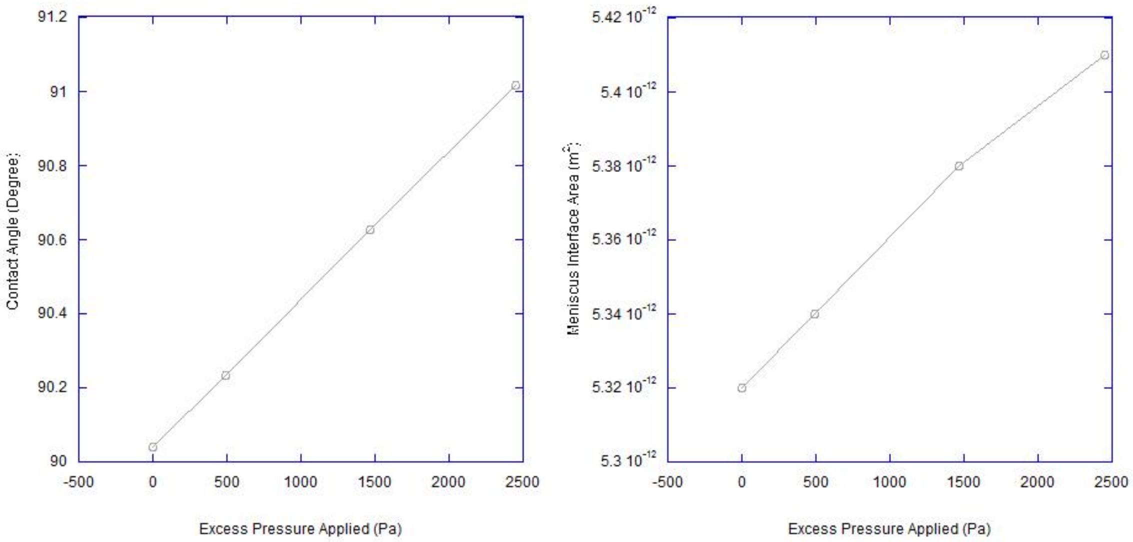

Figure 13. The contact angle change and corresponding meniscus interface area change due to additional pressure applied

3.2 Effect of Additional Pressure Applied to Droplet Growth

The previous studies revealed that the supersaturation condition inside the ECT was not linearly distributed. The supersaturation condition initially took place after a short distance from the inlet and reached its maximum near the middle length (Hering, 2005). The formation of the supersaturated conditions was determined by the energy and mass transfer from the water vapor supplied from the ECT wall. While at the same wall temperature, the evaporation rate of the water vapor determined the amount of high temperature water vapor transferred to the centerline of the tube, which controlled the supersaturation formation location. The additional pressure applied on the interface enlarged the exposure evaporation surface of meniscus, and therefore, the evaporation condition was improved. The enhanced water vapor evaporation condition resulted in the increase of the mass of water vapor. An earlier supersaturation position was expected and led to a longer growth time for a single particle. Since the aerosol flow rate was maintained, the resident time for a particle inside the ECT was fixed. Only when the particles stayed in supersaturation for a longer amount of time could larger condensed droplets be obtained.

Figure 14 shows that the growth condensed droplet sizes increased while the additional pressure was applied on the gas-liquid interface meniscus at the temperature of 348 K (75°C). The additional pressures increased by 490 Pa, 1471 Pa, and 2452 Pa, and the corresponding meniscus evaporation areas were enlarged by 0.34%, 1.03%, and 1.73%, respectively. The grown condensed particles sizes in diameter increased correspondingly to 3.73 μm, 3.75 μm, and 3.8 μm while the droplet size was originally only 3.46 μm.

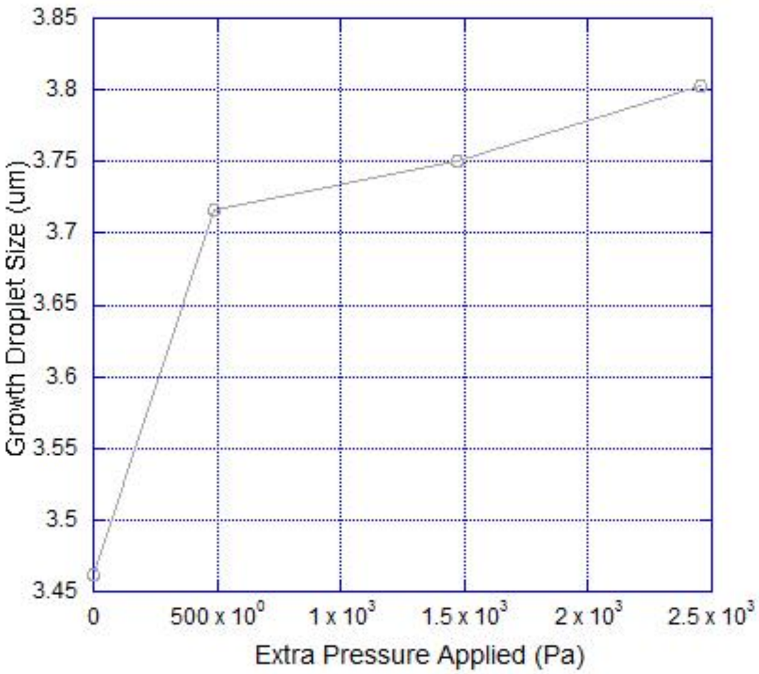

Figure 14. The condensed droplet size change when additional pressure on meniscus at ECT wall temperature 348 K applied.

Repeated experiments have been made with the same aerosol flow rate under the same and different ECT wall temperature conditions (Figure 15). When additional pressure on the meniscus was applied, for the whole range of the ECT wall temperature, the condensed droplet size repeatedly increased. By applying with pressure of 2452 Pa the meniscus area enlarged 1.73%, and the condensed droplet sizes reached at least 10% increase. Also an improvement of 10% on droplet size by enlargement of meniscus area was achieved no matter how low the ECT wall temperature was. Even at the lowest temperature within experiments (55°C, 328 K), the increase percentage remained at about the same level (10% of increase).

To have the same amount of increase at the condensed droplet size, it was necessary to promote the temperature condition by around 3°C.

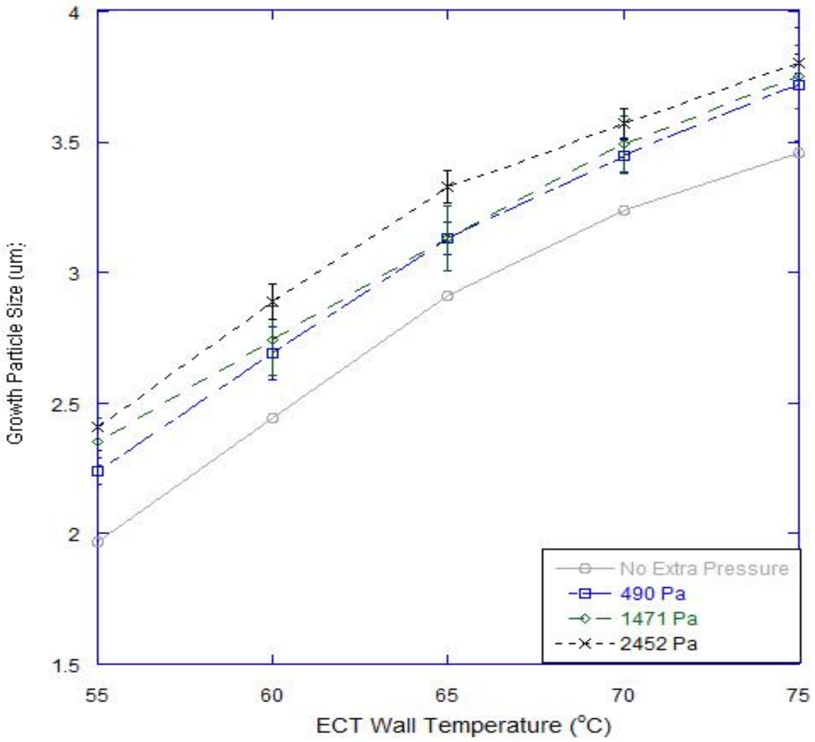

Figure 15. The condensed droplet sizes change when additional pressure on meniscus applied.

The enlargement of the meniscus evaporation area by applying additional pressure on the interface would have an effect on all temperature conditions with the same amount of improvement and the enhancement of 10% which was significant compared with the original growth of droplet sizes from 2 to 4 μm.

3.3 Effect of Additional Pressure Applied to Droplet Detection Efficiency.

Previous condensation droplet growth theories mentioned that only at supersaturation conditions could the droplet begin to grow in the form of heterogeneous nucleation. The droplet detection efficiency for a CPC was determined by the minimum sizes which could be detected among the grown particles.

From the thermodynamics point of view, when a moving particle is encountered with the supersaturation field, it begins to grow and when it is large enough it will be detected. At a critical resident time in the condensation tube (fixed aerosol flow rate), the additional pressure applied on the gas-liquid interface meniscus enlarged the evaporation area and thus increased the evaporation rate. This process improved the mass and energy transfer from the ECT wall to the centerline which led to the advancement of the starting position of the supersaturation field. Thus the growing resident time for each particle increased. This would not only make particles grow bigger, as described previously, but also allow those particles not big enough to be detected to have a longer amount of time to grow. With this being the case, the particles exceeded the detectable limitation size, so that the detection efficiency improved.

Figure 16 shows that experimental results of detection efficiency percentage increase with enlargement of meniscus area while applying additional pressure on gas-liquid meniscus. The condition chosen was at the ECT wall temperature of 65°C (338 K). With the increase of the additional pressure applied on the gas-liquid interface meniscus of every 500 Pa of pressure on average, the detection efficiency was enhanced by around 2 to 3%.

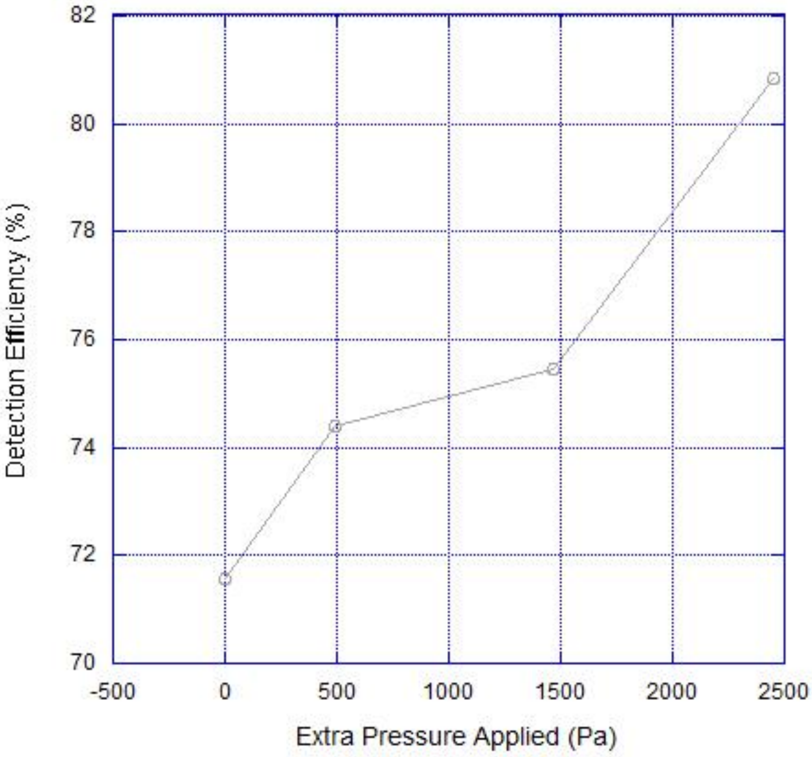

Figure 16. The condensed droplet detection efficiency change when with additional pressure on meniscus at ECT wall temperature 338 K applied.

The droplet detection efficiency discussed, as defined in the previous chapter, is the ratio of the calculated concentration from captured images to the reference CPC readings. From the principle of laser visualization system, only the droplets with diameters larger than the wavelength of the laser (532 nm in this study) can be detected at 100% efficiency. The increase of the detection efficiency mainly resulted from the increase of droplet numbers with longer resident time while staying in the supersaturation field to grow big enough for laser visualization.

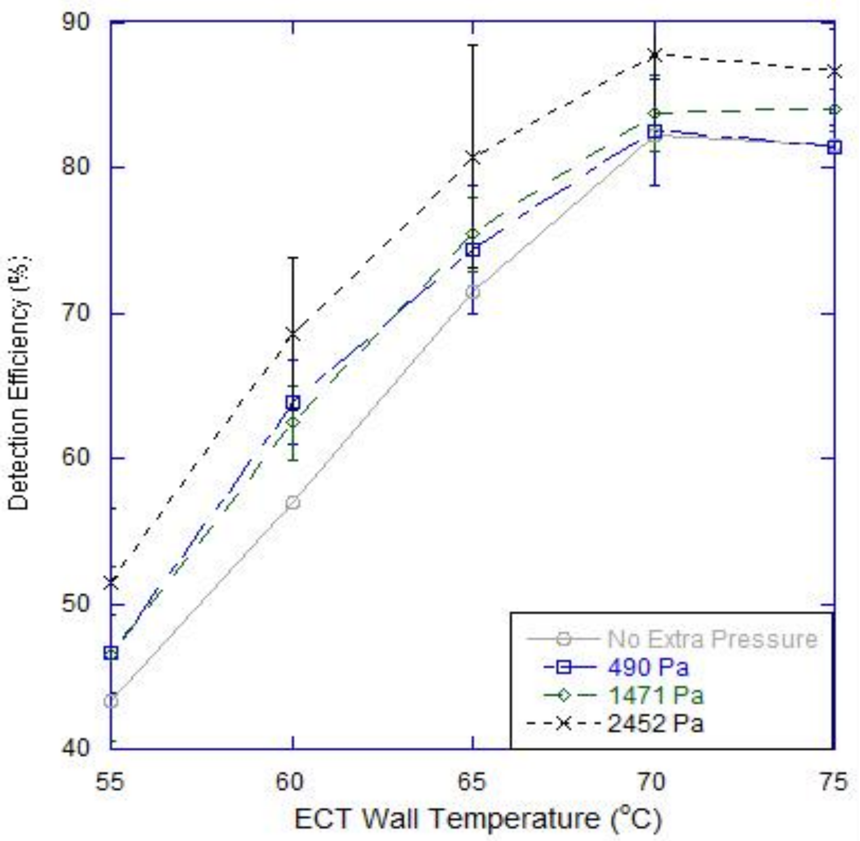

Figure 17. The condensed droplet detection efficiency change when additional pressures on meniscus applied.

Experiments have been conducted under all ECT wall temperature conditions from 55°C to 75°C and the results are shown in Figure 17. For the greatest additional pressure added (24520 Pa) which made 1.74% of evaporation area enlargement, an increase of 5 to 8% enhancement of detection efficiency was observed for all experimental cases. To fulfill the same extent of increase, by the method of increasing wall temperature, an additional 3°C rise should be made. However, for wall temperature, an optimized value existed, which meant when the temperature was higher than such value, the detection efficiency of the condensation tube would not increase due to the condensed droplet heating. In this circumstance, applying additional pressure to enlarge the meniscus evaporation area is an additional method to improve the performance of the ECT.

To show the previous experiment results from a physics point of view, the enhancement effects to the droplet sizes and detection efficiency by the alteration of meniscus gas-liquid interface area is provided in Figure 18. With the pressure applied by 490 Pa, 1471 Pa, and 2452 Pa, the meniscus interface area increased by 0.34%, 1.03%, and 1.73%, respectively. Even though the increase percentages of the evaporation area were small, the enhancement caused on the condensation droplet growth size and detection efficiency of the ECT was significant. When the meniscus area increased by 1.73%, the size enhancement rate and detection efficiency improvement rate were 22.50% and 18.85%, respectively, for the temperature of 328 K (lowest temperature); and were 9.83% and 6.17%, respectively, for the temperature of 348 K (highest temperature). Obviously, it was more effective through the meniscus area enlargement when the temperature was low. Moreover, even at the highest temperature condition, the enlargement of the meniscus area could provide around 8% enhancement for droplet growth size and and 5% for detection efficiency.

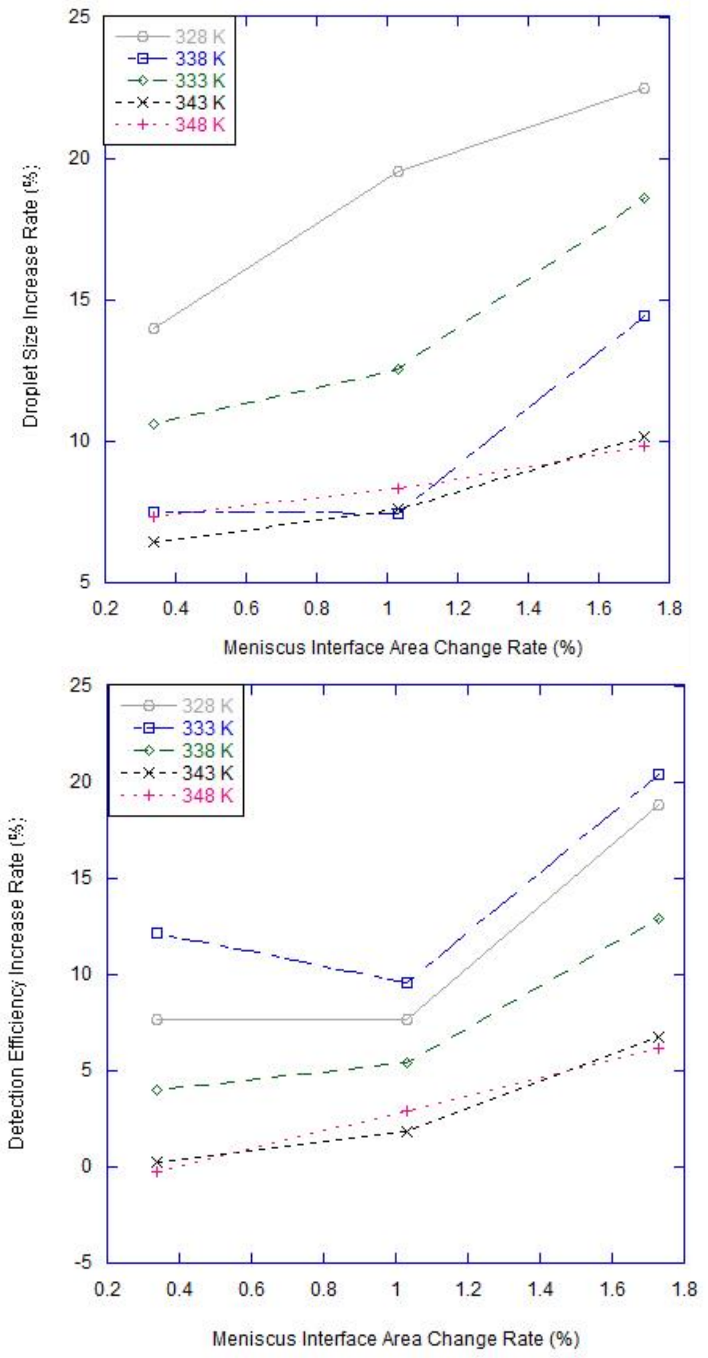

Figure 18. The enhancement of meniscus interface area increase to droplets size and detection efficiency.

4. Conclusion

Supersaturation conditions could be generated with water as working fluid by utilizing a warm wetted column and mixing it with streams of cold air-vapor mixture. Depending on controllable parameters, wall temperature, flow rate, temperature, and capillary pressure on the porous media, the vapor distribution inside the mini-channel causing the particle nucleation may vary. Experimental studies revealed that a 20 nm particle can be grown to 3 to 5 µm in size.

Additional pressure applied on the meniscus interface between liquid and gas phases resulted in larger evaporation area, which enhanced the formation of the supersaturation field, promoted early onset of supersaturation, and increased the spatial extent of supersaturated region in the ECT. This led to the particles growth beginning earlier and lasting longer. Thus, larger droplets were observed and more droplets grew to the detectable size; therefore, the detection efficiency of the CPC was enhanced.

The enlargement of meniscus gas-liquid interface area also had a significant advantage compared to other approaches such as varying other parameters. Under all wall temperature conditions from 55°C to 75°C, the enlargement of meniscus area could supply an additional enhancement to evaporation conditions. In another word, the meniscus interface area enlargement would not influence the thermodynamics condition while improving the performance of the evaporation rate. Not like the parameters such as wall temperature and aerosol flow rate for which the advantage and disadvantage for additional increase need to be balanced, the enlargement of area of gas-liquid interface meniscus could enhance the performance with no shortcomings. Applying an additional pressure is an easy and convenient way to increase the meniscus gas-liquid interface area additional to changing the temperature.

On the other side, the meniscus area has less effect to the condensation performance compared with the parameters like temperature and aerosol flow rate. The enhancement was limited significantly by the material of the porous media of condensation tube since the higher pressure may result in the porous media flooding or even deformation of the material, which would cause the distribution of all thermodynamic conditions to be different and the tube permanently damaged.

Suggested future research studies would be focused on how to apply the additional pressure and to find easier and more practical approaches for application of additional pressure. Also a porous media with high strength and high evaporation rate could be utilized.

References

Agarwal, J. K. and Sem, G. J. (1980). Continuous Flow, Single-Particle-Counting Condensation Nucleus Counter, Journal of Aerosol Science 11:343-357

Ajaev, V. S., Homsy, G. M. (2001). Three-Dimensional Steady Vapor Bubbles in Rectangular Microchannels, Journal of Colloid and Interface Science, 244:1, 180-189

Barrett, J. C., Baldwin T. J. (2000). Aerosol Nucleation and Growth during Laminar Tube Flow: Maximum Saturations and Nucleation Rates, Journal of Aerosol Science 31:633-650

Bricard. J., Delattre, P., Maselaine, G., Pourprix, M. (1976). Detection of ultrafine particles by means of a continuous flux condensation nuclei counter, Fine articles:

Aerosol Generation, Measurement, Sampling and Analysis, B. Y. H. Liu, Ed., Academic Press 565-580

Choi, J. Y. and Son, S. Y. (2009) Growth of Ultrafine Particles Through a Minichannel with Capillary Structure, Proceedings of the Seventh International ASME Conference on Nanochannel, Microchannels and Minichannels ICNMM2009-82248

Clement, C. F. (1985). Aerosol Formation from Heat and Mass Transfer in Vapour-Gas Mixtures. Proceedings of the Royal Society of London. Series A, Mathematical and Physical Sciences 398:307-39.

Davis, T. W., Garimella, S. V., Thermal Resistance Measurement Across a Wick Structure Using a Novel Thermosyphon Test Chamber, Experimental Heat Transfer 21:2, 143-154

De La Mora, J. F. (2011). Heterogeneous Nucleation with Finite Activation Energy and Perfect Wetting: Capillary Theory Versus Experiments with Nanometer Particles, and Extrapolations on the Smallest Detectable Nucleus, Aerosol Science and Technology, 45:4, 543-554

Franklin, L. M., Bika, A. S., Watts, W. F. and Kittelson, D. B. (2010) Comparison of Water and Butanol Based CPCs for Examining Diesel Combustion Aerosols, Aerosol Science and Technology 44:629-638

Glover, A. R., Skippon, S. K., Boyle, R. D. (1995). Interferometric laser imaging for droplet sizing: a method for droplet-size measurement in sparse spray systems, Applied Optics 34:8409-8421

Hanlon, M. A., Ma, H. B., Evaporation Heat Transfer in Sintered Porous Media, ASME Journal of Heat Transfer, 125:644-652

Heidenreich, S. (1994). Condensational droplet growth in the continuum regime-a critical review for the system air-water. Journal of Aerosol Science, 25: 49-59

Hering, S. V. and Stolzenburg, M. R. (2005) A Method for Particle Size Amplification by Water Condensation in a Laminar, Thermally Diffusive Flow, Aerosol Science and Technology 39:428-436

Hering, S. V., Stolzenburg, M. R., Quant, F. R., Oberreit, D. R. and Keady, P. B. (2005). A Laminar-Flow, Water-based Condensation Particle Counter (WCPC), Aerosol Science and Technology 39:659-672

Hinds, W. C. (1999). *Aerosol technology: properties, behavior, and measurement of airborne particles*, Wiley-Interscience 2nd edition

Holm, R. L., Caldow, R., Hairston, P. P., Quant, F. R. and Sem, G. J. (1998) An Enhanced Time-of-Flight Spectrometer that Measures Aerodynamic Size Plus Light-Scattering Intensity, Journal of Aerosol Science 28:511-512

Hoppel, W. A., Twomey, S. and Wojchichowski, T. A. (1979) A Segmented Thermal Diffusion Chamber for Continuous Measurement of CN, Journal of Aerosol Science 10:369-373

Iida, K., Stolzenburg, M. R., McMurry, P. H., Smith, J. N., Quant, F. R., Oberreit, D. R., Keady, P. B., Eiguren-Fernandez, A., Lewis, G. S., Kreisberg, N. M. and Hering, S. V.

(2008) An Ultrafine, Water-Based Condensation Particle Counter and its Evaluation under Field Conditions, Aerosol Science and Technology 42:862-871

Iverson, B. D., Davis, T. W., Garimella, S. V., North, M. T., Kang, S. S., Heat and Mass Transport in Heat Pipe Wick Structures, Journal of Thermophysics and Heat Tranfer 21:2, 392-404

Köhler, H. (1936). The Nucleus in and the Growth of Hygroscopic Droplets, Transactions of the Faraday Society 43:1152

Kupc, A. (2013). Laboratory Characterization of a New Nano-Water-Based CPC 3788 and Performance Comparison to an Ultrafine Butanol-Based CPC3776, Aerosol Science and Technology, 47:2, 183-191

Leaitch, R. and Megaw, W. J. (1982). The diffusion tube; A cloud condensation nucleus counter for use below 0.3% supersaturation, Journal of Aerosol Science 4:297-319

Lee J. Y., Liang H., Son, S.Y. (2011) Condensational droplet growth of ultrafine airborne particles with non-wetting structured tube. AAAR 30th Annual Conference, 2011

Lewis, G., Hering, H. (2013). Minimizing Condentration Effects in Water-Based, Laminar-Flow Condensation Particle Counters, Aerosol Science and Technology, 47:6,645-654

Ma, H. B., Peterson, G. P., Temperature Variation and Heat Transfer in Triangular Grooves with an Evaporation Film, Journal of Thermophysics and Heat Transfer 11:90-97

McMurry, P. H. (2000). The History of Condensation Nucleus Counters, Aerosol Science and Technology 33:297-322.

Mordas, G., Mannien, H. E., Petäjä, T., Aalto, P. P., Hämeri, K. and Kulmala, M. (2008) On Operation of the Ultra-Fine Water-Based CPC TSI 3786 and Comparison with Other TSI Models (TSI 3776, TSI 3772, TSI 3025, TSI 3010, TSI 3007), Aerosol Science and Technology 42:152-158

Morris, S. J. S., (2003) The Evaporating Meniscus in a Channel, Journal of Fluid Mechanics, 494:297-317

Nel, A., Xia, T., Madler, L., Li, N. (2006). Toxic Potential of Materials at the Nanolevel, Science, 311:622-627.

Ragucci, R., Cavaliere, A., Massoli, P. (1990). Drop Sizing by Laser Light Scattring Exploiting Intensity Angular Oscillation in the Mie Regime, Particle & Particle Systems Characterization 7:221-225

Ranjan, R., Murthy, J. Y., Garimella, S. V. (2009). Analysis of the Wicking and Thin-Film Evaporation Characteristics of Microstructures, Journal of Heat Transfer 131:10, 1-11

Ranjan, R., Garimella, S. V., Murthy, J. Y. (2010). Characterization of microstructures for heat transfer performance in passive cooling devices, in: Proceedings of ASME Summer Heat Transfer Conference, Jacksonville, FL, August 10-14, 2008

Seinfeld, J. H. and Pandis, S. N. (2006) *Atmospheric Chemistry and Physics – From Air Pollution to Climate Change*, John Wiley & Sons 2nd edition

Sinclair, D., Hoopes, G. (1975). A continuous flow condensation nucleus counter, Journal of Aerosol Science 6:1-7

Sinclair, D. (1982). Particle Size Sensitivity of Condensation Nucleus Counters. Atmospheric Environment 16:955-958

Spurny, K. R. (2000). Atmospheric Condensation Nuclei P. J. Coulier 1875 and J. Aitken 1880 (Historical review), Aerosol Science and Technology 32:243-248.

Wang, H., Garimella, S. V., Murthey, J. Y. (2007), Characteristics of an Evaporating Thin Film in a Microchannel, International Journal of Heat and Mass Transfer